ADVANCED ENGINEERING MATERIALS
www.aem-journal.com

In Situ High-Energy Synchrotron X-Ray Diffraction Reveals the Role of Texture on the Activation of Slip and Twinning during Deformation of Laser Powder Bed Fusion Ti–6Al–4V

Juan Manuel Vallejos,* Pere Barriobero-Vila, Joachim Gussone, Jan Haubrich, Klemens Kelm, Andreas Stark, Norbert Schell, and Guillermo Requena

The deformation behavior of Ti–6Al–4V processed by laser powder bed fusion (LPBF) is investigated by in situ high-energy synchrotron X-ray diffraction (HEXRD) during uniaxial compression. The initial microstructure of the alloy consists of a fine lamellar α + β microstructure where α lamellae are separated by thin continuous β layers within prior β grains. The anisotropy of the alloy is studied in the deformation direction using samples that are built at the angles of 0°, 45°, and 90° with respect to the LPBF base plate. The sample oriented at 0° presents higher strength–ductility trade-off compared with the conditions oriented at 45° and 90°. The in situ HEXRD experiments continuously reveal the microstructure response during deformation and that the textures for each orientation are associated with a different activation sequence of deformation mechanisms.

1. Introduction

Ti–6Al–4V is the most studied and commercially used Ti-based alloy, occupying more than half of the market share of titanium products.[1,2] The microstructure of this alloy can be tuned by thermomechanical treatments to obtain a wide range of mechanical properties.[3] Also, the excellent corrosion resistance that can be achieved explains the use of Ti–6Al–4V in a wide range of applications, fundamentally in aerospace and biomedical industry.[1]

The traditional manufacturing chain used for Ti–6Al–4V comprises thermomechanical processing followed by machining.[4] The "buy-to-fly" ratio for Ti–6Al–4V aerospace components, namely, the relationship between the weight of the raw material needed to fabricate a component and the weight of the finished part, ranges from 10:1 to 25:1 using conventional manufacturing processes. This usually leads to large amounts of material loss and high machining costs; both can be reduced by metal additive manufacturing (AM). AM is especially attractive for decreasing the production costs of components made of Ti-based alloys, because it can reduce the "buy-to-fly" ratio down to about 1:1.[5] The layer-by-layer AM production forms a CAD model allows the fabrication of near net-shaped metallic components with complex geometries such as load-optimized structures of minimal weight or with integrated inner channels for cooling, which are not achievable with conventional production methods (e.g., casting or machining).

During laser powder bed fusion (LPBF), Ti-based alloys undergo a thermal history consisting of a steep and directional temperature gradient along the building direction. This leads to coarse and columnar prior-β grains strongly textured in the $<100>_{\beta}$ orientation along the building direction.[6–9] In addition, the high cooling rates (at the order of 10^3 °C s^{-1}) produced in LPBF thermal cycles result in the $\beta \rightarrow \alpha'$ (hcp) martensitic transformation.[6,10–14] As a consequence, a microstructure dominated by acicular α′ with Burgers orientation relationship and distributed within prior β grains is usually obtained in as-built LPBF condition.

Dr. J. M. Vallejos
Instituto de Física Rosario
Bv. 27 de febrero 210 bis, 2000 Rosario, Argentina
E-mail: juan.manuel.vallejos@ing.unne.edu.ar

Dr. J. M. Vallejos
Facultad de Ingeniería
Universidad Nacional del Nordeste
Las Heras 727, 3500 Resistencia, Argentina

Dr. P. Barriobero-Vila, Dr. J. Gussone, Dr. J. Haubrich, Dr. K. Kelm, Prof. G. Requena
Institute of Materials Research
German Aerospace Center (DLR)
Linder Höhe, 51147 Cologne, Germany

Dr. A. Stark, Dr. N. Schell
Metallic Structures and Materials Systems for Aerospace Engineering
RWTH Aachen University
52062 Aachen, Germany

Prof. G. Requena
Helmholtz-Zentrum Geesthacht
Max-Planck-Straße 1, 21502 Geesthacht, Germany

The ORCID identification number(s) for the author(s) of this article can be found under https://doi.org/10.1002/adem.202001556.

DOI: 10.1002/adem.202001556

The microstructural defects that arise from LPBF (e.g., porosity) and the nature of α′ martensite (generally seen as a brittle phase) are considered as the cause of poor ductility in as-built LPBF Ti–6Al–4V.[15] Compared with samples with a fully martensitic α′ microstructure, lamellar α + β microstructures usually improve the ductility in Ti–6Al–4V.[10,12,15] To this end, decomposing the metastable α′ phase into stable α and β phases has been the goal of several studies.[6,7,9,16–18] However, it has also been shown that a ductile mechanical response can be achieved in fully α′ or dual α + α′ microstructures, which questions the assumption about the fragile nature of the martensite.[19,20] This behavior was attributed to a higher compatibility, i.e., slip transfer across grain boundaries, between hcp α and α′ grains than in the case of the hcp/bcc α/β interfaces. In opposition, Zheng et al. suggested that the α/β interface plays a key role in the nucleation and propagation of α twins during deformation of Ti–6Al–4V.[21] Despite this, twinning as a plastic deformation mechanism was only reported in very particular cases for this alloy, such as high-cycle fatigue or high strain rates.

The deformation modes that can be activated during deformation of LPBF Ti–6Al–4V are a complex issue. In addition to the microstructural features mentioned earlier, they depend on crystallographic texture, i.e., on the load direction.[22–25] In this work, in situ high-energy synchrotron X-ray diffraction (HEXRD) is carried out during compressive deformation to determine the sequence of activation of deformation mechanisms and its correspondence with the texture obtained in Ti–6Al–4V manufactured by LPBF. The deformation modes of LPBF Ti–6Al–4V are investigated for conditions deformed at 0°, 45°, and 90° with respect to the LPBF building platform. The in situ time-resolved experiments using HEXRD allow for continuous tracking of the deformation mechanisms.

2. Experimental Section

2.1. Laser Powder Bed Fusion

LPBF of a Ti–6Al–4V (wt%) grade 23 powder alloy was carried out in argon 5.0 atmosphere using an SLM280HL machine (SLM Solutions Group AG, Lübeck, Germany). The chemical composition of the powder according to the specification provided by AP&C is 0.11 wt% O, 6.39 wt% Al, 3.80 wt% V, and 0.19 wt% Fe. Oxygen was determined by the powder provider AP&C using inert gas fusion following ASTM E1409, and the metallic elements were determined according to ASTM E2371 by direct current plasma emission spectroscopy. The temperature of the build platform was set to 200 °C. The powder alloy was produced by gas atomization and consisted of spherical particles of a size distribution $D_{10} = 22$ µm, $D_{50} = 34$ µm, and $D_{90} = 46$ µm, measured by the standard method ASTM B822. Cubic samples of $10 \times 10 \times 10$ mm^3 were built using a chess scanning strategy. The laser pattern for the bulk material consists of chess domains, where the scanning vectors between these domains present a relative rotation of 90°.[26] The LPBF processing parameters are summarized in **Table 1**. The volume energy density was calculated using Equation (1). The LPBF strategy aimed at applying an intensified intrinsic heat treatment (IHT) to promote decomposition of α′ martensite into stable α and β phases.[7] This microstructure is sought to increase the ductility of Ti–6Al–4V.[10,12,15]

Table 1. LPBF parameters used for the processing of the samples.

Laser power P [W]	Scanning velocity v [mm s^{-1}]	Hatch distance h [µm]	Focal offset distance F [mm]	Layer thickness d [µm]	Volume energy density E_v [J mm^{-3}]
250	1000	40	0	30	208

For compression testing, LPBF cubic samples were machined into cylindrical specimens of 5.5 mm length and 3.5 mm diameter. To study the anisotropy of the alloy, the cylindrical samples were machined with the compression axis at 0°, 45°, and 90° with respect to the base plate plane of the LPBF machine (hereinafter, 0°, 45°, and 90° conditions, respectively). A schematic image of the compression directions of the samples with respect to the building platform is shown in **Figure 1**.

$$E_v = \frac{P}{v \cdot h \cdot d}\ [\mathrm{J\,mm^{-3}}] \quad (1)$$

where E_v is the volume energy density; v is the scanning velocity; h is the hatch distance, and d is the layer thickness.

2.2. In Situ HEXRD during Uniaxial Compression

In situ HEXRD during uniaxial compression was performed in transmission mode (sample thickness = 3.5 mm) at the beamline P07-HEMS of PETRA III (Deutsches Elektronen-Synchrotron, DESY, Hamburg, Germany).[27] High-energy X-rays (30–1000 keV) such as provided by synchrotron radiation sources offer high penetration into matter allowing nondestructive bulk investigations of materials.[28] Thus, these so-called hard X-rays permit analyzing the samples of Ti alloys with a thickness of several mm in transmission mode. In this study, this configuration is combined with a 2D detector allowing fast acquisition of complete sets of the Debye–Scherrer rings in a single beam shot. In this study, this configuration is combined with a 2D detector allowing fast acquisition of complete sets of the Debye–Scherrer rings in a single beam shot. The incident X-ray beam was positioned at the center of the samples before and during deformation. A PerkinElmer XRD 1621 detector acquired the Debye–Scherrer rings during deformation at the intervals of 0.5 s/image.

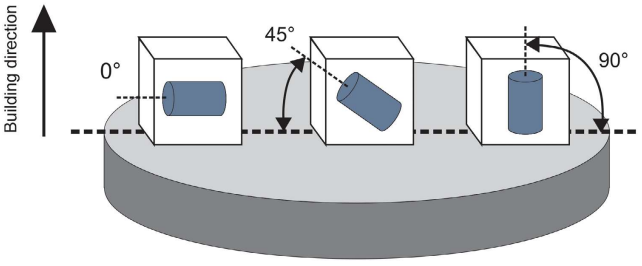

Figure 1. The samples investigated were manufactured in build directions of 0° (0°), 45° (45°), and 90° (90°) with respect to the base plate of the LPBF machine.

The compression tests were carried out at room temperature using a modified dilatometer Bähr 805A/D equipped with a deformation unit.[29,30] The cylindrical samples were compressed at a strain rate of 0.002 s^{-1}. No buckling of the samples was observed during deformation. The effect of the dilatometer stiffness on the phase's macrostrains is assumed to be negligible. An illustrative diagram of the experimental setup is shown in **Figure 2**a.

2.3. Data Processing

To investigate the evolution of the diffraction images obtained in situ by HEXRD during deformation, the acquired Debye–Scherrer rings were unrolled and converted into Cartesian coordinates (Azimuth angle ψ, 2θ), as shown in Figure 2b. Then, the unrolled {h k l} reflection was cut from the diffraction image, as indicated by the green dotted-line rectangle in Figure 2b. Using the software ImageJ, the intensity sum of Bragg reflections was projected on the ψ–ε plane.[31] This step is shown in Figure 2c. Finally, a normalized color-coded 2D image is plotted, corresponding to the evolution of {h k l} Bragg reflection intensity for the Azimuthal range 0°–360° as a function of strain during uniaxial compression (Figure 2d).

The software MAUD was used for Rietveld and texture analyses of the diffraction patterns.[32] An extended Williams–Imhof–Matthies–Vinel (E-WIMV) algorithm integrated in MAUD was used for texture analysis.[32,33] The moment pole stress was used as a stress model for the Rietveld refinement of the images acquired under compression.[34,35] The instrumental parameters of the HEXRD setup were obtained from a LaB_6 powder standard. The Schmid factors (SFs) of the α phase were calculated using the software MTEX, and the crystal lattice parameters were obtained from Rietveld refinements.[36]

Sections of 20° (±10° with respect to the load) direction were taken from the Debye–Scherrer rings (Figure 2a) to calculate the lattice strains during deformation according to Equation (2).[37] The 2θ variations of individual {h k l} reflections in the load direction were considered for this analysis. Similarly, the calculation of the full width at half maximum (FWHM) were determined for the cake portions of 20° in the load direction by single peak fitting (pseudo-Voigt approximation).

$$\varepsilon_{hkl} = \frac{d_{hkl} - d^0{}_{hkl}}{d^0{}_{hkl}} \quad (2)$$

where ε_{hkl} is the lattice strain of a {h k l} plane family; $d^0{}_{hkl}$ and d_{hkl} are the plane spacings for the {h k l} family before and during deformation, respectively.

2.4. Microstructure Characterization

Scanning electron microscopy (SEM) in backscattered electron mode (BSE) was used to characterize the microstructure of the samples in the as-built condition. The SEM studies were performed using an FEI Helios-Nanolab600i dual-beam microscope (FEI, Hillsboro, OR, USA). The specimens were prepared by

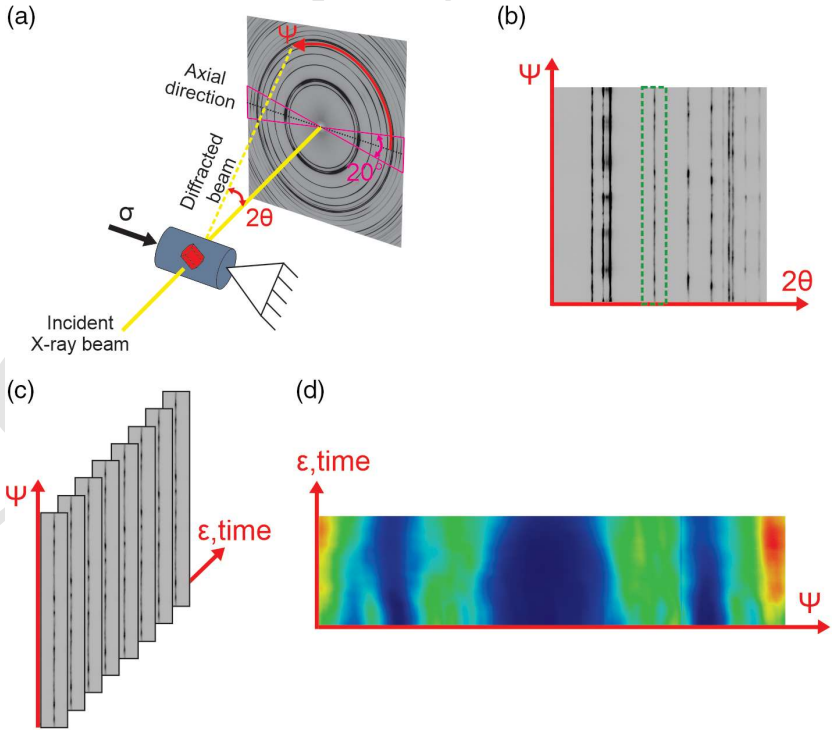

Figure 2. a) In situ HEXRD during uniaxial compression: experimental setup. b) Debye–Scherrer rings unrolled and converted into Cartesian coordinates (Azimuthal angle ψ, 2θ). c) Example of the evolution as a function of strain for a single {h k l} reflection shown in the selected inset (green dashed line) of (b). d) Normalized color-coded 2D image corresponding to the evolution of an {h k l} Bragg reflection intensity for the Azimuthal range 0°–360° as a function of strain during uniaxial compression.

grinding and polishing using a TegraPol machine with 3 μm diamond and SiO_2 suspension. Thin-foil samples were prepared for transmission electron microscopy (TEM) by focused ion beam using an FEI Helios Nanolab 600i setup. The samples were examined with a Philips Tecnai F30 transmission electron microscope (Philips, Netherlands) operated at 300 keV.

3. Results

Figure 3a,b shows the initial microstructure of the LPBF as-built condition. Prior-β grain boundaries are highlighted by dashed lines in Figure 3a. Due to the high energy density and the focal offset distance (0 mm) used during the LPBF, a total decomposition of the α′ martensite into α + β is expected, according to the literature.[10] Figure 3b shows that the microstructure obtained is characterized by this decomposition of α′. However, as some acicular plates appear to remain in several parts of the specimen, we cannot assure that the total decomposition of the martensite took place. In addition, both α and α′ are hcp phases with similar lattice parameters, and they cannot be reliably distinguished using HEXRD. For this, they will be referred to as α hereinafter. Layers of β can be observed in light gray (see arrows). The lamellar microstructure is composed of fine β layers decorating the α

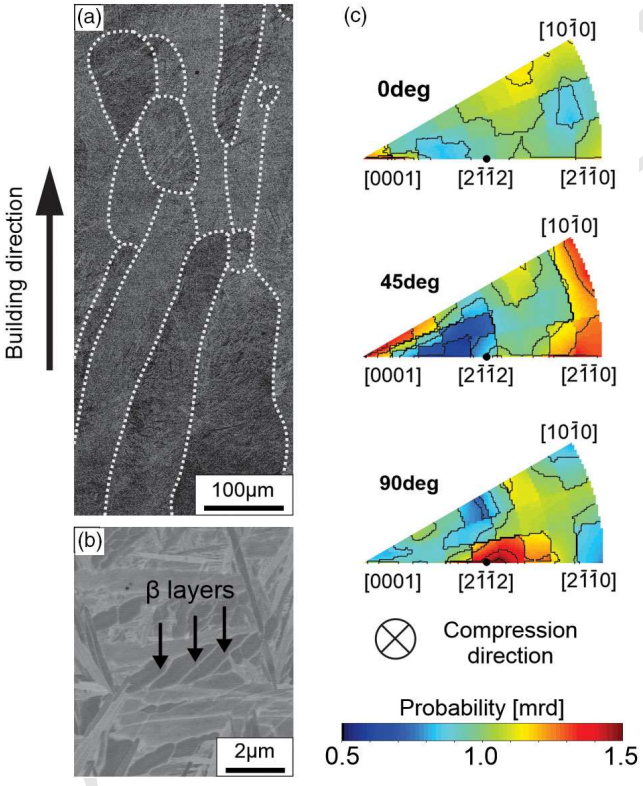

Figure 3. a) SEM-BSE image of the as-built LPBF condition. The prior-β grains are highlighted by dashed lines. b) SEM-BSE image with major magnification, where β layers are indicated by arrows. c) Inverse pole figures of α for 0°, 45°, and 90° orientations in the compression direction. The building direction is vertical for 0° and 45° from the compression direction for 45° and coincident with the compression direction for 90° condition.

grains. These results correlate well with previous investigations reporting this effect using high energy density during LPBF.[7,26]

Figure 3c shows the inverse pole figures of α for 0°, 45°, and 90° in the compression direction. In 0° orientation, the maximum intensities are located close to the basal and prismatic planes. On the other hand, in the specimen at 45°, the maximum intensities are mainly found on the right-hand side of the stereographic triangle, i.e., close to the [10$\bar{1}$0]α and [2$\bar{1}\bar{1}$0]α directions, as well as close to the basal plane. In contrast, for 90°, the directions near (2$\bar{1}\bar{1}$2)α are those found most closely aligned to the load direction.

The true stress–strain curves obtained from the room temperature compression tests are plotted in **Figure 4**a. The 0° orientation shows higher ductility and strength than the other two conditions. To analyze the work hardening behavior of the three studied conditions, the evolution of the strain hardening rate (SHR) is shown as dotted-line curves as a function of true strain (Figure 4a). It can be observed that the SHR for the 0° condition is higher than for 45° and 90° during the entire deformation. Figure 4b shows the ultimate strength and deformation at break for the three studied orientations. The strength–ductility trade-off is maximum for 0°. On the opposite, the 45° condition presents the lowest ductility and strength.

Figure 5a–c shows the evolution of the basal {0004}α reflections as a function of strain during compression for the 0°, 45°, and 90° conditions, respectively (Azimuthal range = 0°–360°). The {0004}α reflection was chosen instead of {0002}α due to the overlapping of the latter with the {110}β reflection. The corresponding true stress–strain and SHR–true strain curves are also plotted on the right-hand side of the 2D color-coded plots. The horizontally built 0° specimen (Figure 5a) shows reflections around $\psi \approx 15°$, 110°, 195°, and 315° that begin to vanish at $\varepsilon \approx 0.05$. Simultaneously, new reflections become visible at $\psi \approx 40°$, 220°, and 260°. These sudden shifts are related to instantaneous rotations of a significant fraction of the crystals due to twinning.[38] Some reflections ($\psi \approx 40°$ and 220°) also show a continuous and slight shift of around 15° along the Azimuth angle, denoting the activation of slip-driven grain rotation as an acting plastic deformation mechanism.

In the 45° condition, {0004}α reflections at $\psi \approx 110°$ and 280° present continuous broadening, as the strain increases (Figure 5b). This indicates that slip plays an important role as a plastic deformation mechanism in this condition. Also, the reflections at $\psi \approx 110°$ and 280° present an increase in intensity at $\varepsilon \approx 0.05$, whereas those at $\psi \approx 0°$ and 30° decrease their intensity. These effects are indications that strain-induced twinning may occur from $\varepsilon \approx 0.05$.

The 90° condition presents a peak broadening, which starts at $\varepsilon \approx 0.03$ up to the end of deformation in reflections at $\psi \approx 150°$ and 330° (Figure 5c). In addition, at $\varepsilon \approx 0.05$, a sudden and remarkable intensity increase takes place in reflections located at $\psi \approx 55°$ and 235° and to a lesser extent at $\psi \approx 150°$ and 330°. This suggests the activation of twinning from this strain level.

Figure 5a–c indicates that both mechanisms of plastic deformation, namely, slip and twinning, can be present in the three investigated conditions. The TEM image corresponding to the 0° post-mortem sample is shown in **Figure 6**a. This figure provides the evidence of the activation of twinning-induced plasticity

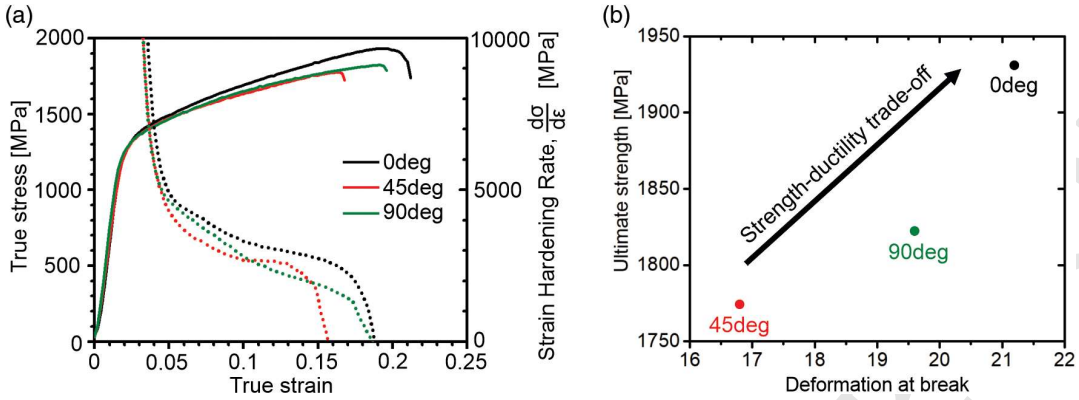

Figure 4. a) True stress–strain curves obtained during uniaxial compression. The SHR is also plotted as dotted-line curves. b) Strength–ductility trade-off for the investigated conditions.

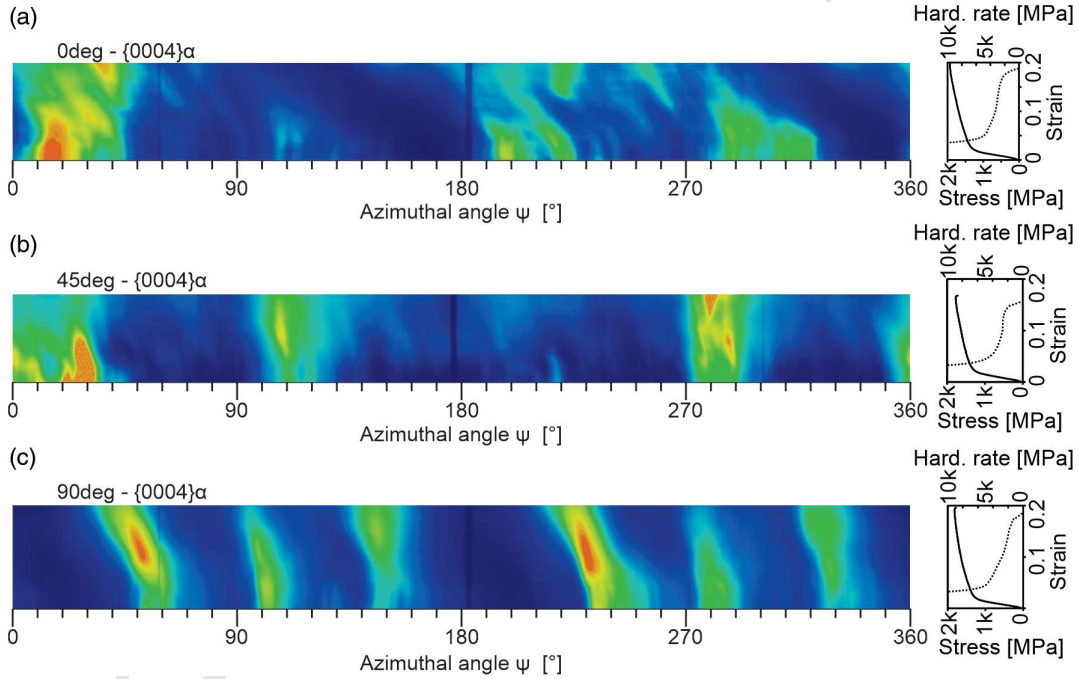

Figure 5. Color-coded 2D plots corresponding to the evolution of {0004}α for the Azimuthal range 0°–360° during uniaxial compression: a) 0°, b) 45°, and c) 90°. The true stress–strain and SHR–true strain curves are shown on the right-hand side of the 2D plots.

phenomenon. The strain-induced α twins were observed in several zones of the LPBF compressed specimen. The crystallographic orientation between the α matrix and the twin is clearly observed in the $[\bar{2}110]\alpha$ zone axis shown in Figure 6b. The rotation of about 60° and the $[\bar{2}110]\alpha$ rotation axis are compatible with $\{10\bar{1}1\} < 10\overline{12} >$ compression twinning. Although there is evidence of both twinning and slip mechanisms in the three conditions studied, the activation sequence and the mode that dominate the plastic deformation in each case seem to differ and are analyzed in the following.

The evolution of FWHM of the prismatic $\{01\bar{1}0\}\alpha$, basal $\{0002\}\alpha$, and pyramidal $\{01\bar{1}1\}\alpha$ planes is presented in **Figure 7** to provide further insight into the mechanisms active during deformation. An increase in FWHM is generally related to peak broadening associated with the variation of type-III microstrains provoked by lattice defects, such as dislocations and staking faults.[39] In the 0° orientation, the peak broadening gradually increases from $\varepsilon \approx 0.02$, as deformation progresses. This implies a continuous increase in the density of defects generated by slip in the α crystals. The basal plane undergoes the largest peak widening. In the 45° condition, the peaks broaden in a similar manner as in the previous case, reaching a maximum at $\varepsilon \approx 0.12$, and then remaining constant until fracture. The broadening of $\{0002\}\alpha$ at the onset of plastic deformation is faster for

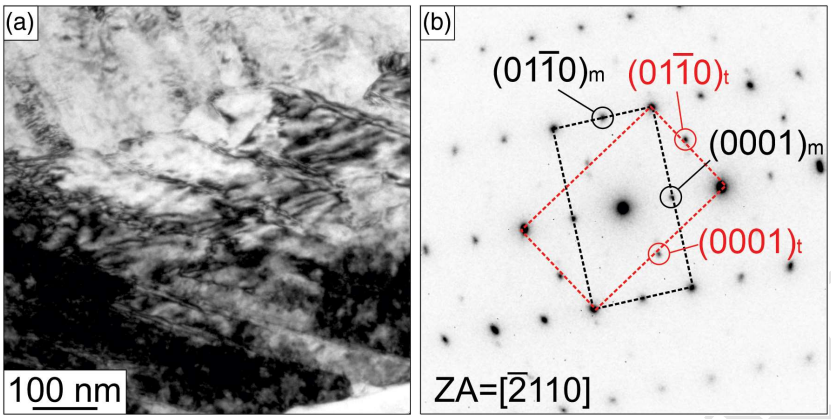

Figure 6. a) TEM image corresponding to the 0° post-mortem sample. b) Electron diffraction pattern of the [$\bar{2}$110]α zone axis taken from the center region in (a).

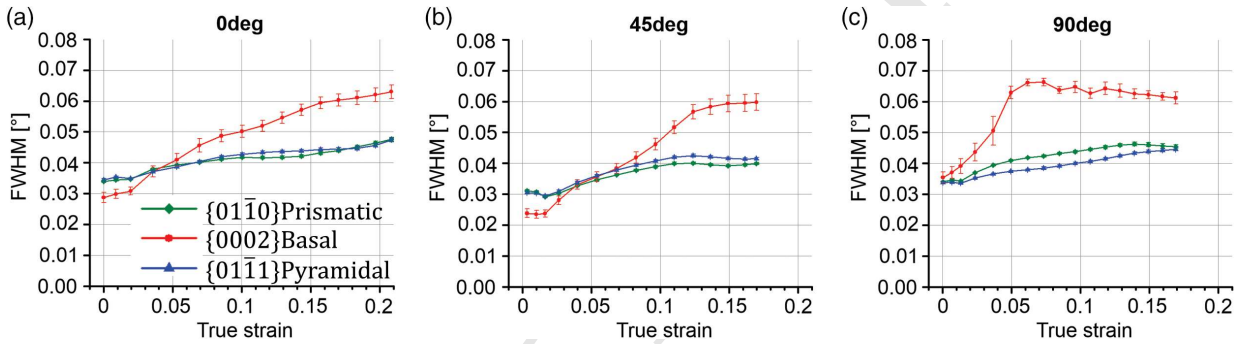

Figure 7. Evolution of FWHM along the compression direction for prismatic {01$\bar{1}$0}α, basal {0002}α, and pyramidal {01$\bar{1}$1}α planes during deformation for: a) 0°, b) 45°, and c) 90° conditions.

the 90° orientation than for the other conditions. The FWHM of this reflection reaches a maximum at $\varepsilon \approx 0.05$ and remains constant. On the other hand, the peak broadening of {01$\bar{1}$0}α and {01$\bar{1}$1}α undergoes a lower increase until fracture.

The FWHM evolution shown in Figure 7 indicates different basal slip activities between orientations. While the 0° condition exhibits a continuous slip activity throughout the experiment, the 45° and 90° orientations show a stepwise behavior; i.e., the FWHM reaches a plateau. Moreover, in the 90° condition, the alloy presents a very strong basal slip activity at the onset of plastic deformation. Thereafter, the FWHM of the basal plane remains relatively constant at $\varepsilon \approx 0.06$.

It is expected that grains undergoing twin formation experience stress relaxation.[40–43] Thus, the evolution of representative lattice strains of the α phase in the compression direction is plotted in **Figure 8** to identify the strain range during which twinning takes place. In the 0° condition, a slight but continuous relaxation is observed in the plastic period at $\varepsilon > 0.05$ for the prismatic and pyramidal planes. At $\varepsilon > 0.19$, right before fracture, all planes experience an abrupt strain release. On the other hand, lattice relaxation was not observed in planes corresponding to 45° orientation at any strain level. The 90° condition presents an abrupt stress relaxation of the basal plane between $\varepsilon \approx 0.05$ and 0.10, which suggests a strong twinning formation in this stage of plastic deformation. From $\varepsilon \approx 0.10$, the lattice strains of basal and prismatic planes undergo a slight increase until the sample fails.

These results correlate well with those shown in Figure 5a–c. In the 0° condition, a combination of twinning and slip in α crystals takes place throughout the entire range of plastic deformation. Twinning-induced plasticity is revealed by sudden changes in intensity of some reflections (Figure 5a) and lattice strain relaxation (Figure 8a). On the other hand, slip is evidenced by the widening of the diffraction spots shown in Figure 5a and 7a, and by the inclination along the ψ-axis of some reflections, which is an indication of grain rotation (Figure 5a).[44]

The 90° condition shows slip as the dominant mechanism at the onset of plastic deformation (Figure 5c and 7c). Twinning is then active from $\varepsilon \approx 0.05$ up to $\varepsilon \approx 0.10$: this can be deduced from the sudden intensity increase in reflections located at $\psi \approx 55°$ and 235° in Figure 5c and from the lattice strain relaxation shown in Figure 8c.

In the 45° orientation, slip is the main plastic deformation mode as evidenced by peak broadening, grain rotation, and the plateau of lattice strains shown in Figure 5b, 7b, and 8b. As a very minor contribution, twinning seems to be activated at approximately $\varepsilon > 0.05$, because some reflections suddenly change in intensity, as shown in Figure 5b.

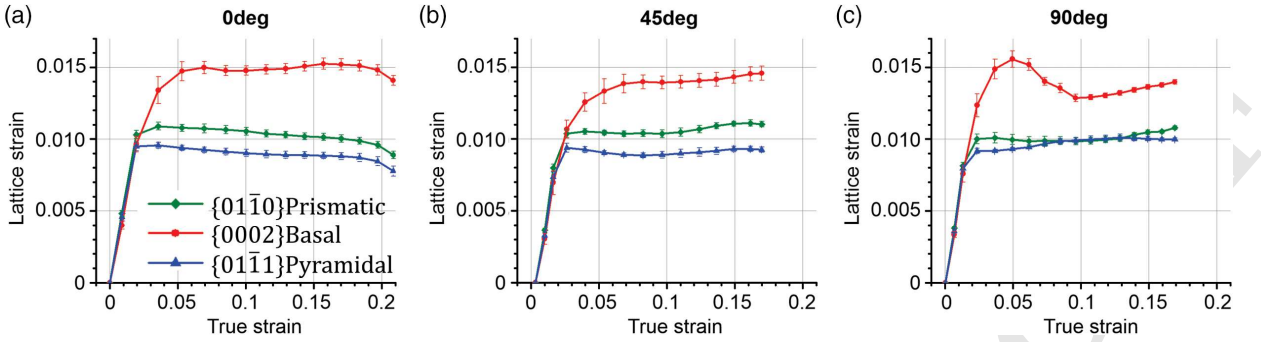

Figure 8. Evolution of lattice strains along the compression direction for prismatic {01$\bar{1}$0}α, basal {0002}α, and pyramidal {01$\bar{1}$1}α planes during deformation for: a) 0°, b) 45°, and c) 90° conditions.

4. Discussion

4.1. Role of Initial Texture on Deformation Behavior

The microstructural monitoring by HEXRD during compression tests of Ti–6Al–4V in the three conditions studied shows that both slip and strain-induced twinning can be activated during deformation. However, the relevance and activation sequence of these mechanisms depends on the particular load direction and the initial texture.

In the 0° condition, slip is activated at the onset of plastic deformation. This is evidenced by the increase in FWHM of the α reflections of basal, prismatic, and pyramidal planes, as shown in Figure 7a. At slightly higher strains (from $\varepsilon \approx 0.05$), twinning starts to assist slip, as shown by the sudden changes in intensity observed in Figure 5a. Similarly, in the 90° condition, the slip activity that occurs from the onset of the plastic deformation coexists with twinning, mainly between $\varepsilon \approx 0.05$ and $\varepsilon \approx 0.10$, as it is shown in Figure 5c, 7c, and 8c. The trigger for the initiation of twinning may be the hardening that occurs in the alloy due to the increasing of dislocation density by slip, which is also related to an increment in the critical resolved shear stress (CRSS).[41] The work hardening of the slip systems are expected to be different in each case, and as a consequence, the stress required to activate each slip system will increase differently with strain. This phenomenon was described by Tomé et al. using a modified Vocé formulation to calculate the strain hardening effect in each slip system as a function of the accumulated shear strain.[45] This can cause some grains to become prone to twinning when the CRSS of the slip system that dominated the plastic deformation up to that point reaches a critical value. On the other hand, in the 45° condition, it can be assumed that slip is the dominant mechanism, because a continuous increase in FWHM is observed (Figure 7b), and the twinning indications are weaker than in 0° and 90° conditions (no relaxation of lattice strains, Figure 8b, and low activity of intensity changes, Figure 5b).

The Schmid's law establishes a geometrical criterion to evaluate the inclination of crystallographic systems to deform via slip and twinning. This law is generally used for single crystals under uniaxial load and for slip as deformation mechanism. However, it can also be used to qualitatively evaluate the tendency of the grains to deform by a particular deformation mode.[46] **Figure 9**a,b shows the SFs as a function of the crystallographic orientation for basal, prismatic, and pyramidal slip systems, and for the main types of deformation twinning systems that can occur in α titanium.[47] Each one of these twinning modes is associated with a particular axis (r) and angle of rotation (ω). The latter represents the misorientation between the parent grain and the twin. While tensile twinning introduces a positive strain along the c-axis of the parent α grain, compression twinning implies a negative component of strain along the c-axis.[48] Tensile twins are often found in specific microstructural areas of a material subjected to compression when a crystal has the c-axis oriented perpendicular to the compression axis, and its extension is, therefore, required to accommodate deformation. The directional dependence of twinning for hcp crystals can be observed in the SF corresponding to twinning systems in Figure 9b. The compression twinning system presents maximum SF when the compression direction is parallel to [0001]α, and decreases, as the c-axis moves away from the load direction. In contrast, the SF of tensile twinning systems has a maximum when the c-axis is perpendicular to the compression direction. It should be noted that the CRSS for the basal and prismatic slip systems in Ti–6Al–4V is very similar to each other, and they are much lower than that for the pyramidal system.[49] This implies that for a grain with a high SF for the pyramidal slip system, the other two slip systems can be activated first, because their CRSS is smaller. The evolution of FWHM of the diffraction peaks shown in Figure 7 clearly suggests a higher dislocation activity in the basal plane than in the prismatic and pyramidal ones. This can be a consequence of the low CRSS for the basal slip system and numerous grains with a high SF in the samples.

By comparing the initial texture presented in the IPF of Figure 9c with the SF in Figure 9a,b, the 0° orientation presents a texture with the majority of the grains prone to activate several deformation systems: {10$\bar{1}$1}α compression and {10$\bar{2}$1}α tensile twinning as well as prismatic and pyramidal slip. This texture distribution with favorably oriented grains for twinning or slip activation explains the mechanical behavior of this condition at the beginning of the compression test. The initial orientation of grains in this condition, prone to trigger both tensile and compression twinning modes, indicates that both processes may take place during deformation. This agrees with Figure 5a, where several sudden intensity changes can be seen for this condition, although it is not possible to identify a defined angle of rotation. This could indicate

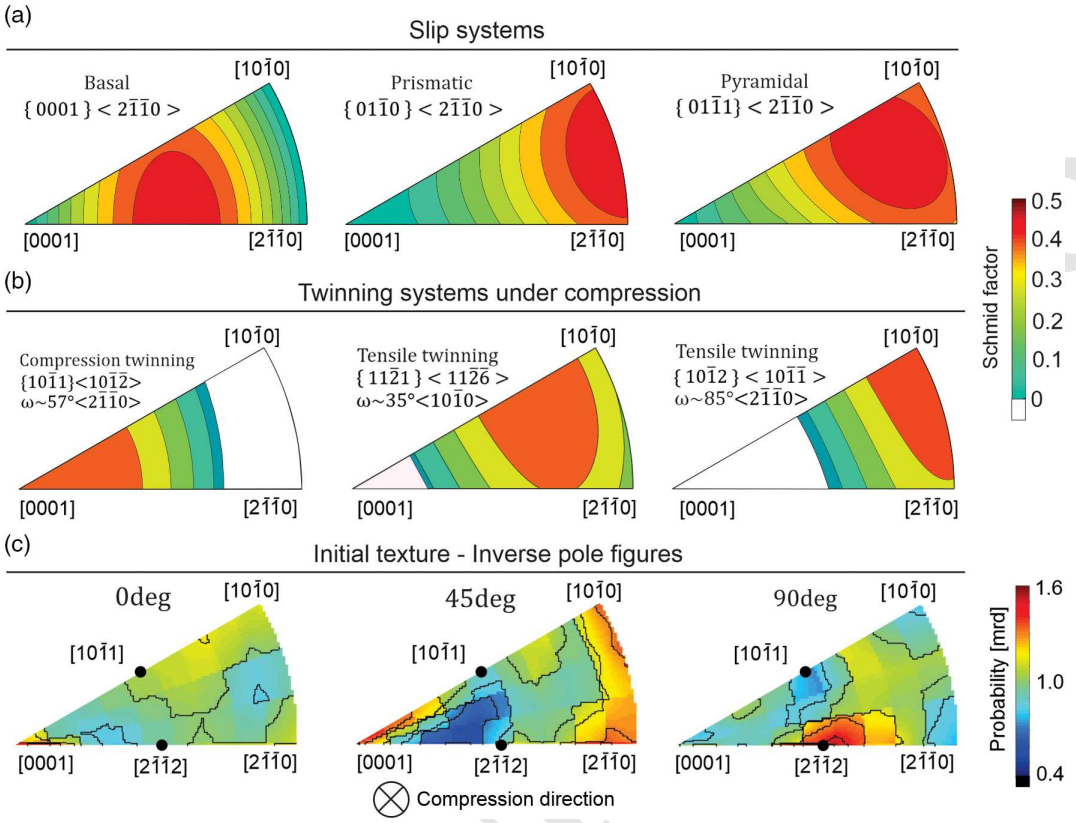

Figure 9. SFs as a function of crystallographic orientation for: a) basal, prismatic, and pyramidal slip systems and b) {10$\bar{1}$1}α, {11$\bar{2}$1}α, and {10$\bar{1}\bar{2}$}α twinning systems under compression. c) Inverse pole figures of α showing the initial texture for the three investigated conditions.

that more than one twinning system is activated. It is also possible that these twinning systems are being activated sequentially, as it is widely reported for pure Ti and α-Ti alloys.[47,49–52]

The initial texture in the 45° orientation is very favorable for activating the prismatic slip system, as it can be observed in the IPF shown in Figure 9c. Although some grains are well oriented to activate {10$\bar{1}$1}α compression and {10$\bar{1}\bar{2}$}α tensile twinning systems, the prismatic slip system is associated with a low CRSS. Thus, it is plausible that the latter dominates over the twinning deformation modes.[49]

The deformation mechanisms that can be activated at the beginning of compression for the 90° condition are slip in the basal system as well as pyramidal slip and {10$\bar{2}$1}α tensile twinning, as observed by comparing Figure 9a–c. The initial texture, strongly oriented with the [2$\bar{1}\bar{1}$2]α parallel to the load direction, indicates that the initial deformation mechanism that governs at the onset of plastic range is slip in the basal plane system. This can be seen in the rapid broadening of the {0002}α reflection during the initial stage of plastic deformation, as it is shown in Figure 7c. The grains favorably oriented for {11$\bar{2}$1}α tensile twinning may be responsible for the strain-induced twinning activity, higher than in the 45° condition but lower than in the 0° condition, as it is shown in Figure 5, 7, and 8. Compression twinning is initially restricted in this condition, because there are not many grains with the *c*-axis oriented in the load direction at the beginning of deformation.

Although the strain relaxation seems to be larger in the 90° condition than in the 0° condition for the basal plane, it is concentrated in the range $\varepsilon \approx 0.05$–0.1 for the former condition (Figure 8a,c). This implies that the twinning in the 90° sample is mostly concentrated in this deformation range. Conversely, in the 0° orientation, the pyramidal and prismatic planes are relaxed less abruptly than that observed in the basal plane of the 90° sample but continuously throughout the plastic deformation range. This indicates that the twinning remains active throughout the compression test in the 0° condition.

4.2. Texture Evolution during Compression

A sequential texture development is generally observed in materials where twinning makes a major contribution to plastic deformation.[52] This is related to the reorientation of domains within grains during the nucleation and growth of twins. As shown in Figure 5a, the 0° condition seems to show the most remarkable texture variation. The IPF of this sample at different strain levels is shown in **Figure 10**a to better understand the evolution of texture during compression. The texture changes considerably during deformation in the 0° orientation. The most remarkable variation is the decrease in intensity near the [10$\bar{1}$0]α direction. These orientations have high SF for both tensile twinning modes, {11$\bar{2}$1}α and {10$\bar{1}\bar{2}$}α, as it is shown in Figure 9. This is associated with the intensity increase at the base of

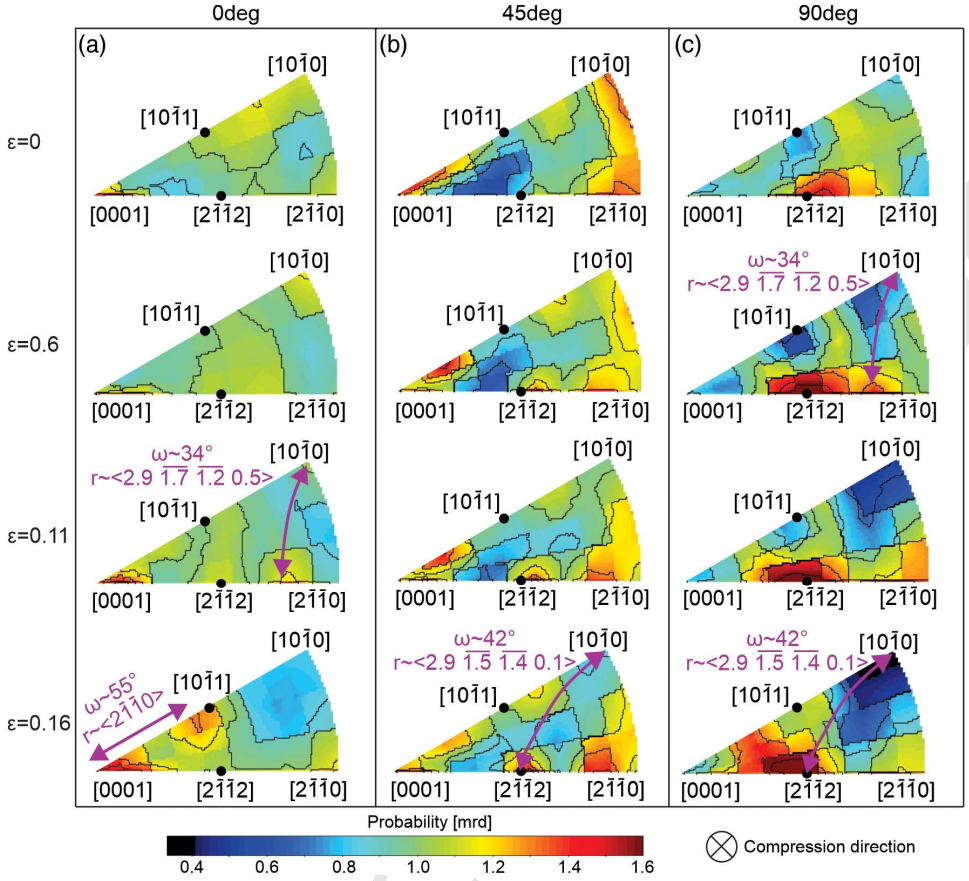

Figure 10. Inverse pole figures at representative strain levels showing the texture evolution during uniaxial compression for: a) 0°, b) 45°, and c) 90° conditions.

stereographic triangle, between $\{2\bar{1}\bar{1}2\}\alpha$ and $\{2\bar{1}\bar{1}0\}\alpha$, as indicated by the arrow in Figure 10a at $\varepsilon = 0.11$. This figure shows that this increment in intensity can be related to the activation of $\{11\bar{2}1\}\alpha$ tensile twinning in crystals oriented near $[10\bar{1}0]\alpha$, with a shift of about 35° and $\langle 2\bar{1}\bar{1}0\rangle\alpha$ as the rotation axis. The calculated angle of rotation ω is 34°, very close to the theoretical angle, and the axis of rotation r is $\langle 2.9\,\bar{1}.7\,\bar{1}.2\,0.5\rangle$, only 8° away from the $\langle 2\bar{1}\bar{1}0\rangle$ theoretical axis. A different increase in intensity can be observed near the $[10\bar{1}1]\alpha$ direction at $\varepsilon = 0.16$. This can be related to a slight decrease in intensity near $[0001]\alpha$, which are the grains with the highest SG for compression twinning. The rotation that exists between these two directions is ≈55° around $\langle 2\bar{1}\bar{1}0\rangle$, which is almost exactly the rotation of $\{10\bar{1}1\}\alpha$ compression twinning mode. The stress–strain curve for this condition shows a strength–ductility trade-off higher than the other two orientations. We suggest that this is related to the combined activation of slip and strain-induced twinning, which also produces a high SHR.

Less significant texture changes than in the previous case were observed in the 45° condition (Figure 10b). This is compatible with slip as the dominant mode of plastic deformation. A slight increase in intensity near $[2\bar{1}\bar{1}2]\alpha$ is compatible with the formation of $\{11\bar{2}1\}\alpha$ tensile twinning in grains oriented close to $[10\bar{1}0]\alpha$. The rotation between the parent grains and twins is represented by the calculated angle of rotation ω of 42° (7° away from the theoretical one) and the axis of rotation $r\,\langle 2.9\,\bar{1}.5\,\bar{1}.4\,0.1\rangle$ (1.5° of difference with the $\langle 2\bar{1}\bar{1}0\rangle$ theoretical axis). In the 45° condition, the tendency to activate the prismatic slip system in detriment of the other deformation modes, fundamentally the twinning systems, seems responsible for the low elongation at break and SHR achieved.

The initial texture of the 90° condition, with most of the grains oriented with the $[0001]\alpha$ *c*-axis far from the load direction, restricts the activation of compression twinning (Figure 10c). However, many crystals are prone to activate basal slip and $\{11\bar{2}1\}\alpha$ tensile twinning. These two mechanisms govern plastic deformation in this condition. Similar rotations to those shown in the two previous cases were found. These are compatible with $\{11\bar{2}1\}\alpha$ tensile twinning in grains oriented close to $[10\bar{1}0]\alpha$ direction. The texture evolution has similarities to that observed in Figure 10a for the 0° condition: an intensity decrease can be observed close to the $[10\bar{1}0]\alpha$, i.e., a region that corresponds to a high SF for $\{11\bar{2}1\}\alpha$ tensile twinning (Figure 9b). As fewer grains are prone to activate twinning in the 90° condition compared with the 0°, a lower strength–ductility trade-off is obtained in the former.

Despite the fact that the three studied conditions present an initial texture with grains prone to activate the two tensile

twinning systems, only $\{11\bar{2}1\}\alpha$ twinning seems to be active during compression. In pure Ti, the governing twinning mode is $\{10\bar{1}2\}$.[47] However, as the content of Al increases, this deformation mechanism is abruptly restricted.[53] This was attributed to a higher stacking fault energy and yield stress with increasing Al.[53] In this sense, the 6 wt% of Al in Ti–6Al–4V may be responsible for the difference in the activation of twinning mechanisms compared with pure Ti.

For pure Ti, it is commonly known that twinning plays a fundamental role during plastic deformation. However, there are limited reports of twinning in Ti–6Al–4V and only in particular cases such as high strain rates.[21,22,54,55] This study points to twinning as an important deformation mode for this alloy when produced by LPBF. The existence of the twinning-induced plasticity mechanism as a dominant mode of deformation in the samples studied in this work may be a direct consequence of the manufacturing method. Materials processed by high-energy LPBF exhibit a high density of crystallographic defects that can act as nucleation sites for twinning and element partitioning that can modify the stacking fault energy of the α phase.[18] Furthermore, the partial decomposition of α′ into $\alpha+\beta$ due to the intensified IHT applied during LPBF in this work generates a clear α/β interface surface that plays a key role in the nucleation and propagation of α twins during deformation of Ti–6Al–4V.[21] On the other hand, a favorable initial texture is fundamental for the activation and propagation of the different twinning modes.

In summary, **Figure 11**a–c shows the dominant deformation mechanisms observed for each deformation stage in the 0°, 45°, and 90° conditions, respectively. For the 0° orientation, a combination of four mechanisms governs the plastic deformation: basal and prismatic slip, $\{10\bar{1}1\}\alpha$ compression twinning, and $\{11\bar{2}2\}\alpha$ tensile twinning. The relatively larger amount of domains oriented close to $[10\bar{1}0]\alpha$ and $[0001]\alpha$ compared with the 45° and 90° conditions, and the coexistence of the four deformation modes throughout the entire range of plastic deformation makes it possible to achieve a higher strength–ductility trade-off in the 0° condition. On the other hand, slip in the basal system dominates the initial plastic deformation in the 90° orientation, followed by a combination of slip and $\{11\bar{2}1\}\alpha$ tensile twinning, fundamentally in $\varepsilon \approx 0.05$–0.1. Basal slip is considered to be the dominant mechanism in the second stage of deformation, whereas twinning assists it to accommodate compression strain. This assumption is based on the fact that this condition showed less signs of twinning than in the previous case, and that the initial texture is well oriented to activate slip in the basal plane. The mechanism that dominates the plastic deformation in the 45° orientation is slip in the α prismatic system. Twinning plays a secondary role, and as a consequence, the deformation at break and the ultimate strength are lower than in the previous cases.

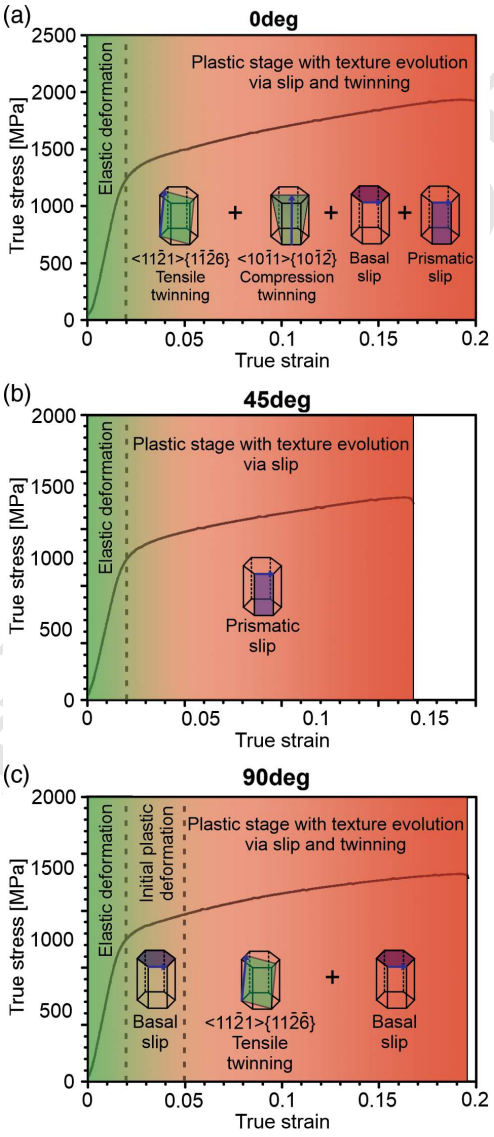

Figure 11. Plastic deformation mechanisms dominating in each deformation stage indicated on the true stress–strain curves of: a) 0°, b) 45°, and c) 90° conditions.

5. Conclusion

In this work, the deformation mechanisms under compression of Ti–6Al–4V processed by LPBF were investigated in situ using HEXRD. To this purpose, samples oriented at 0°, 45°, and 90° with respect to the LPBF build plate were investigated. These are three conditions with different initial textures of the α phase with respect to the load direction. In situ compression tests were performed during HEXRD to monitor the evolution of the microstructure during deformation. The following conclusions can be drawn.

1) A microstructure derived from the partial decomposition of α′ into α grains and β layers was obtained within prior β grains by LPBF as a consequence of the intensified IHT applied during LPBF. The prior β grains have predominantly columnar shapes, whereas some globular grains were also observed. 2) The highest ultimate strength and deformation at break were obtained in the 0° condition. On the contrary, the lower strength–ductility trade-off was observed for the 45° condition. The higher deformation at break obtained in the 0° and 90° conditions is a consequence of the substantial contribution of strain-induced twinning to the

plastic deformation of the alloy. 3) The initial texture plays an important role in the resulting strength–ductility trade-off. An initial texture favorable for $\{11\bar{2}1\}\alpha$ tensile and $\{10\bar{1}0\}\alpha$ compression twinning systems, with several grains oriented with $[10\bar{1}0]\alpha$ and $[0001]\alpha$ in the load directions, produces a sequential and synergistic activation of slip and twinning deformation modes that lead to an improved mechanical response. On the other hand, an initial texture for which prismatic slip dominates deformation, with grains oriented near $[10\bar{1}0]\alpha$ and $[2\bar{1}\bar{1}0]\alpha$ orientations, restricts the mechanical performance of LPBF Ti–6Al–4V. 4) A fast evolution of texture was observed in the conditions where twinning produced a substantial contribution to plastic deformation, i.e., 0° and 90°. The texture evolution in this conditions shows sudden grain rotations, compatible with both $\{11\bar{2}1\}\alpha$ tensile twinning and $\{10\bar{1}0\}\alpha$ compression twinning. On the other hand, the texture during compression in the 45° build orientation shows minor changes, as expected from a condition in which slip in prismatic system dominates plastic deformation. Also, the rotations in this condition are compatible with $\{11\bar{2}1\}\alpha$ tensile twinning.

The results obtained in this work show that there are still windows of opportunity to adjust the strength–ductility trade-off of LPBF Ti–6Al–4V by tuning initial texture and exploiting the combined effects of slip and twinning.

Acknowledgements

The Deutsches Elektronen-Synchrotron (DESY) is acknowledged for the provision of synchrotron radiation facilities in the framework of the proposal I-20191042.

Conflict of Interest

The authors declare no conflict of interest.

Data Availability Statement

The data that support the findings of this study are available from the corresponding author upon reasonable request.

Keywords

additive manufacturing, high-energy synchrotron X-ray diffraction, laser powder bed fusion, textures, titanium alloys, twinning-induced plasticity

Received: December 31, 2020
Revised: April 6, 2021
Published online:

[1] C. Leyens, M. Peters, *Titanium and Titanium Alloys: Fundamentals and Applications*, Wiley-VCH, Weinheim, Germany **2003**.
[2] C. Cui, B. Hu, L. Zhao, S. Liu, *Mater. Des.* **2011**, *32*, 1684.
[3] G. Lütjering, *Mater. Sci. Eng.: A* **1998**, *243*, 32.
[4] G. Lütjering, J. C. Williams, *Titanium*, Springer, New York **2007**.
[5] R. Huang, M. Riddle, D. Graziano, J. Warren, S. Das, S. Nimbalkar, J. Cresko, E. Masanet, *J. Cleaner Prod.* **2016**, *135*, 1559.
[6] T. Vilaro, C. Colin, J. D. Bartout, *Met. Mat. Trans. A* **2011**, *42A*, 3190.
[7] P. Barriobero-Vila, J. Gussone, J. Haubrich, S. Sandlöbes, J. Da Silva, P. Cloetens, N. Schell, G. Requena, *Materials* **2017**, *10*, 268.
[8] S. Q. Wu, Y. J. Lu, Y. L. Gan, T. T. Huang, C. Q. Zhao, J. J. Lin, S. Guo, J. X. Lin, *J. Alloys Compd.* **2016**, *672*, 643.
[9] G. Kasperovich, J. Haubrich, J. Gussone, G. Requena, *Mater. Des.* **2016**, *105*, 160.
[10] W. Xu, M. Brandt, S. Sun, J. Elambasseril, Q. Liu, K. Latham, K. Xia, M. Qian, *Acta Mater.* **2015**, *85*, 74.
[11] J. J. Yang, H. C. Yu, J. Yin, M. Gao, Z. M. Wang, X. Y. Zeng, *Mater. Des.* **2016**, *108*, 308.
[12] W. Xu, E. W. Lui, A. Pateras, M. Qian, M. Brandt, *Acta Mater.* **2017**, *125*, 390.
[13] J. J. Yang, J. Han, H. C. Yu, J. Yin, M. Gao, Z. M. Wang, X. Y. Zeng, *Mater. Des.* **2016**, *110*, 558.
[14] X. Y. Zhang, G. Fang, S. Leeflang, A. J. Bottger, A. A. Zadpoor, J. Zhou, *J. Alloys Compd.* **2018**, *735*, 1562.
[15] D. Agius, K. I. Kourousis, C. Wallbrink, *Metals* **2008**, *8*, 75.
[16] C. De Formanoir, S. Michotte, O. Rigo, L. Germain, S. Godet, *Mater. Sci. Eng.: A* **2016**, *652*, 105.
[17] V. Popov, A. Katz-Demyanetz, A. Garkun, G. Muller, E. Strokin, H. Rosenson, *Procedia Manuf.* **2018**, *21*,, 125.
[18] J. Haubrich, J. Gussone, P. Barriobero-Vila, P. Kürnsteiner, E. Jägle, D. Raabe, N. Schell, G. Requena, *Acta Mater.* **2019**, *167*, 136.
[19] H. Matsumoto, H. Yoneda, K. Sato, S. Kurosu, E. Maire, D. Fabregue, T. J. Konno, A. Chiba, *Mater. Sci. Eng.: A* **2011**, *528*, 1512.
[20] A. Zafari, K. Xia, *Mater. Res. Lett.* **2018**, *6*, 627.
[21] X. Zheng, S. Zheng, J. Wang, Y. Ma, H. Wang, Y. Zhou, X. Shao, B. Zhang, J. Lei, R. Yang, X. Ma, *Acta Mater.* **2019**, *181*, 479.
[22] A. W. Bowen, *Mater. Sci. Eng.* **1979**, *40*, 31.
[23] M. Simonelli, Y. Y. Tse, C. Tuck, *Mater. Sci. Eng.: A* **2014**, *616*, 1.
[24] F. Wang, S. Williams, P. Colegrove, A. Antonysamy, *Metall. Mater. Trans. A* **2013**, *44*, 968.
[25] T. Scharowsky, V. Juechter, R. Singer, C. Körner, *Adv. Eng. Mater.* **2015**, *17*, 1573.
[26] P. Barriobero-Vila, K. Artzt, A. Stark, N. Schell, M. Siggel, J. Gussone, J. Kleinert, W. Kitsche, G. Requena, J. Haubrich, *Scr. Mater.* **2020**, *182*, 48.
[27] N. Schell, A. King, F. Beckmann, T. Fischer, M. Müller, A. Schreyer, *Mater. Sci. Forum* **2014**, *772*, 57.
[28] P. Staron, A. Schreyer, H. Clemens, S. Mayer, *Neutrons and Synchrotron Radiation in Engineering Materials Science: From Fundamentals to Applications*, Wiley-VCH, Weinheim, Germany **2017**.
[29] P. Staron, T. Fischer, T. Lippmann, A. Stark, S. Daneshpour, D. Schnubel, E. Uhlmann, R. Gerstenberger, B. Camin, W. Reimers, E. Eidenberger, H. Clemens, N. Huber, A. Schreyer, *Adv. Eng. Mater.* **2011**, *13*, 658.
[30] P. Barriobero-Vila, J. Gussone, K. Kelm, J. Haubrich, A. Stark, N. Schell, G. Requena, *Mater. Sci. Eng.: A* **2018**, *717*, 134.
[31] C. A. Schneider, W. S. Rasband, *Nat. Methods* **2012**, *9*, 671.
[32] L. Lutterotti, S. Matthies, H. R. Wenk, A. J. Schultz, J. Richardson, *J. Appl. Phys.* **1997**, *81*, 594.
[33] L. Lutterotti, D. Chateigner, S. Ferrari, J. Ricote, *Thin Solid Films* **2004**, *450*, 34.
[34] S. Matthies, *Text. Microstruct.* **1996**, *25*, 229.
[35] S. Matthies, H. G. Priesmeyer, M. R. Daymond, *J. Appl. Crystallogr.* **2001**, *34*, 585.
[36] R. Hielscher, H. Schaeben, *J. Appl. Cryst.* **2008**, *41*, 1024.
[37] O. Muránsky, D. G. Carr, M. R. Barnett, E. C. Oliver, P. Sittner, *Mater. Sci. Eng.: A* **2008**, *496*, 14.
[38] K. Yan, D. G. Carr, M. D. Callaghan, K.-D. Liss, H. Lia, *Scr. Mater.* **2010**, *62*, 246.
[39] R. L. Rothman, J. B. Cohen, *J. Appl. Phys.* **1971**, *42*, 971.

[40] L. Wu, S. R. Agnew, D. W. Brown, G. M. Stoica, B. Clausen, A. Jain, D. E. Fielden, P. K. Liaw, *Acta Mater.* **2008**, *56*, 3699.
[41] B. Clausen, C. N. Tome, D. W. Brown, S. R. Agnew, *Acta Mater.* **2008**, *56*, 2456.
[42] H. Abdolvand, M. R. Daymond, *Acta Mater.* **2012**, *60*, 2240.
[43] S. R. Kada, P. A. Lynch, J. A. Kimpton, M. R. Barnett, *Acta Mater.* **2016**, *119*, 145.
[44] D. Canelo-Yubero, C. Poletti, F. Warchomicka, J. Daniels, G. Requena, *J. Alloys Compd.* **2018**, *764*, 937.
[45] C. N. Tomé, P. J. Maudlin, R. A. Lebensohn, G. C. Kaschner, *Acta Mater.* **2001**, *49*, 3085.
[46] E. Schmid, W. Boas, *Kristallplastizität: Mit Besonderer Berücksichtigung der Metalle*, Springer, Berlin, Germany **1935**.
[47] N. Bozzolo, L. Chan, A. D. Rollett, *J. Appl. Cryst.* **2010**, *43*, 596.
[48] X. Liao, J. Wang, J. Nie, Y. Jiang, P. Wu, *MRS Bull.* **2016**, *41*, 314.
[49] F. Bridier, P. Villechaise, J. Mendez, *Acta Mater.* **2005**, *53*, 555.
[50] W. Tirry, M. Nixon, O. Cazacu, F. Coghe, L. Rabet, *Scr. Mater.* **2011**, *64*, 840.
[51] S. Xu, L. S. Toth, C. Schuman, J.-S. Lecomte, M. R. Barnett, *Acta Mater.* **2017**, *124*, 59.
[52] S. Xu, M. Gong, C. Schuman, J.-S. Lecomte, X. Xie, J. Wang, *Acta Mater.* **2017**, *132*, 57.
[53] A. Fitzner, D. G. L. Prakash, J. Q. da Fonseca, M. Thomas, S.-Y. Zhang, J. Kelleher, P. Manuel, M. Preuss, *Acta Mater.* **2016**, *103*, 341.
[54] D. G. Leo Prakash, R. Ding, R. J. Moat, I. Jones, P. J. Withers, J. Quinta da Fonseca, M. Preuss, *Mater. Sci. Eng.: A* **2010**, *527*, 5734.
[55] H. Z. Zhong, X. Y. Zhang, S. X. Wang, J. F. Gu, *Mater. Des.* **2018**, *144*, 14.

Advanced Engineering Materials

Editorial Office:
Wiley-VCH GmbH
Boschstraße 12, 69469 Weinheim
Germany

Tel.: +49 (0) 6201-606-581 or 238
Fax: +49 (0) 6201 – 606 – 510
Email: aem@wiley-vch.de

Reprint Order Form

Manuscript No.: _____
Customer No.: (if available) _____
Purchase Order No.: _____
Author: _____

Charges for Reprints in Euro (excl. VAT), prices are subject to change. Minimum order 50 copies.

No. of pages	50 copies	100 copies	150 copies	200 copies	300 copies	500 copies
1– 4	345,—	395,—	425,—	445,—	548,—	752,—
5– 8	490,—	573,—	608,—	636,—	784,—	1077,—
9–12	640,—	739,—	786,—	824,—	1016,—	1396,—
13–16	780,—	900,—	958,—	1004,—	1237,—	1701,—
17–20	930,—	1070,—	1138,—	1196,—	1489,—	2022,—
every additional 4 pages	147,—	169,—	175,—	188,—	231,—	315,—

Information regarding VAT: The charges for publication of *cover pictures /reprints/issues/poster/Video abstracts/* are considered to be "supply of services" and therefore subject to German VAT. However, if you are an institutional customer outside Germany, the tax can be waived if you provide us with the valid VAT number of your company. Non-EU customers may have a VAT number starting with "EU" instead of their country code, if they are registered with the EU tax authorities. If you do not have a valid EU VAT number and you are a taxable person doing business in a non-EU country, please provide a certification from your local tax authorities confirming that you are a taxable person under local tax law. Please note that the certification must confirm that you are a taxable person and are conducting an economic activity in your country. **Note:** certifications confirming that you are a tax-exempt legal body (non-profit organization, public body, school, political party, etc.) in your country do not exempt you from paying German VAT.

Please send me send bill me for

☐ no. of reprints

☐ high-resolution PDF file (330 Euro excl. VAT)
E-mail address: _____

❖ Special Offer:
If you order 200 or more reprints you will get a PDF file for half price.

Please note: It is not permitted to present the PDF file on the internet or on company homepages.

VAT number: _____

Mail reprints / copies of the issue to:

_____
_____
_____
_____
_____

Send bill to:

_____
_____
_____
_____

Cover Posters (prices excl. VAT)
Posters of published covers are available in two sizes:

☐ DinA2 42 x 60 cm / 17 x 24in (one copy: 39 Euro)

☐ DinA1 60 x 84 cm / 24 x 33in (one copy: 49 Euro)

Postage for shipping (prices excl. VAT)
overseas +25 Euro
within Europe +15 Euro

☐ **I will pay by bank transfer**

☐ **I will pay by credit card**

VISA, Mastercard and AMERICAN EXPRESS
For your security please use this link (Credit Card Token Generator) to create a secure code Credit Card Token and include this number in the form instead of the credit card data. Click here:
https://www.wiley-vch.de/editorial_production/index.php

CREDIT CARD TOKEN NUMBER

						V									

_____
Date, Signature

Wiley-VCH GmbH–A company of John Wiley & Sons, Inc. -
Location of the Company: Weinheim - Trade Register: Mannheim, HRB 736569
Managing Directors: Sabine Haag and Dr. Guido F. Herrmann

WILEY-VCH